

A Study of Space-Time Discretizations for the Dirac Equation

Robert Vaselaar¹, Hyun Lim¹, Jung-Han Kim¹

¹ *Department of Mathematics and Statistics, South Dakota State University, Brookings, SD 57007*

We study several numerical discretization techniques for the one-space plus one-time dimensional Dirac equation, including finite difference and space-time finite element methods. Two finite difference schemes and several space-time finite elements function spaces are analyzed with respect to known analytic solutions. Further we propose a finite element discretization along the equations' characteristic lines, creating diamond-shaped elements in the space-time plane. We show that the diamond shaped elements allow for physically intuitive boundary conditions, improve numerical efficiency, and reduce the overall error of the computed solution as compared to the other finite difference and space-time finite element discretizations studied in this paper.

I. INTRODUCTION

The Dirac equation governs all spin- $\frac{1}{2}$ particles, known as fermions. While solutions to the Dirac equation may be used to derive quantifiable predictions of particle behavior from quantum physics, these solutions are sometimes difficult to find in experimentally interesting scenarios. Numerical methods for the Dirac equation may be able to bridge some of the gap between theoretical and experimental particle physics [1, 2].

These include many finite difference based methods for lattice quantum chromodynamics, such as the Dirac Wilson equation [3] which have been used in conjunction with modern numerical methods such as Krylov subspace solvers [4, 5] and scalable additive Schwarz preconditioners [6]. The limitations of these methods are also well known and include the inability to reconcile all limitations simultaneously. This is particularly important when considering the problem of fermion doubling, a condition where the number of particles considered must naturally double for each space-time dimension included on the lattice, and chiral symmetry, which is usually broken by most numerical methods that prevent fermion doubling [7, 8].

Other numerical methods for the Dirac equation include radial formulations created to investigate the energy spectrum of heavy atomic ions [9–12]. These are based on the Dirac equation in the presence of a coulomb potential resulting a relativistic eigenvalue problem, using both finite difference and finite element numerical methods.

The finite element method has also been used to calculate the propagation of free fermions in space. Analysis of the finite element method combined with Crank-Nicholson time stepping scheme demonstrates that solutions may show inconsistent and impossible physical behavior, such as superluminal propagation, depending on the step size and propagation method used [13]. Since using Lagrangian interpolation elements in one dimension are algebraically similar to using finite differences, it is also natural that this choice of function space has the same problems of fermion doubling and numerical instability as its finite difference relative[13]. In this implementation, physically consistent behavior of the particle depended on particle momentum, finite element size, and time step size chosen.

In this paper, several implicit space-time discretizations based on the finite difference and Galerkin methods are presented. This presentation will show that simulation behavior is directly affected by choice of discretization method and function space. The problem domain is then rotated by 45° in the space-time plane, forming diamond-shaped tensor elements, and the solution is recalculated using the rotated domain. This rotated domain shows substantially reduced error and improved performance when compared to the other space-time discretizations listed here. The goal of this research is to create a discrete form of the Dirac equation that shows good agreement with the analytic solution as well as low error and the absence of faster-than-light propagation. Further, we would prefer a solution that does not modify the original Dirac operator in order keep as many of its original physical properties as possible.

This paper is organized as following; First we present the weak form of the gauge-free Dirac Equation in section II. In section III two space-time finite difference and one finite element method are presented along with their numerical results to observe their behavior and performance. Then in section IV three finite element discretizations using space-time tensor elements are presented along with their numerical results. Sources of possible simulation error are also presented and analyzed. Proceeding from the discussion of error we propose our diamond-shaped approach in section V and show how this approach addresses the errors observed and improves simulation efficiency. We conclude by discussing future research opportunities in Section VI.

II. SPACE-TIME METHODS

A. Weak Formulation of the Dirac Equation

The one dimensional Dirac operator may be expressed as follows

$$\hat{D} = (-i\hbar I \partial_t - i\hbar c \sigma_1 \partial_x + mc^2 \sigma_0) \quad (1)$$

where σ_0, σ_1 are the usual Pauli matrices defined as

$$\sigma_0 = \begin{bmatrix} 1 & 0 \\ 0 & -1 \end{bmatrix} \quad (2)$$

$$\sigma_1 = \begin{bmatrix} 0 & 1 \\ 1 & 0 \end{bmatrix} \quad (3)$$

Here the Pauli matrices are chosen such that the variables x and t form a Minkowski space-time, which an essential relationship in the Dirac equation.

In this case we will consider the initial value problem given by

$$\hat{D}\hat{\Psi} = 0 \text{ on } \Omega \times [0, T] \quad (4)$$

$$\hat{\Psi}(\cdot, 0) = \hat{\Psi}^0 \quad (5)$$

In the gage-free case analytic solutions may be computed directly which will give us a basis for comparison for our numerical results.

Using the continuous time Galerkin method the weak form may be expressed as follows. The objective is to find $\Phi, \Psi \in H_0^1(\Omega \times [0, T])$ such that

$$\int_{\Omega \times [0, T]} \hat{\Psi}^* \hat{D} \hat{\Psi} ds = 0 \quad (6)$$

III. NUMERICAL RESULTS OF DIFFERENT NUMERICAL APPROACHES

In this section we will show some results from two finite difference approaches and one finite element method to the Dirac equation. These are the central difference method, the staggered finite difference formulation, and the finite element method using triangular finite elements. In each method we observe significant non-physical effects in the space-time boundary value problem introduced previously. For the sake of comparison, we refer the reader to figure 1 which shows the analytic solution to the space-time boundary value problem proposed above.

A. Central Difference Discretization

For an implicit implementation of the two-dimensional Dirac equation using the finite difference method, the integral used in the bilinear form above may be replaced with a double summation

$$\sum_i^N \sum_j^N \Phi_i \left(i\hbar \begin{bmatrix} 1 & 0 \\ 0 & -1 \end{bmatrix} \partial_t + i\hbar \begin{bmatrix} 0 & 1 \\ -1 & 0 \end{bmatrix} \partial_x - m \right) \Psi_j \delta_{ij} = 0 \quad (7)$$

$$\text{where } \delta_{ij} = \begin{cases} 1 & \text{when } i = j \\ 0 & \text{when } i \neq j \end{cases} \quad (8)$$

Often referred to as the naive discretization, the matrix in this approach is built according to equation 7. Here we use the following central difference definitions for the partial derivative operators.

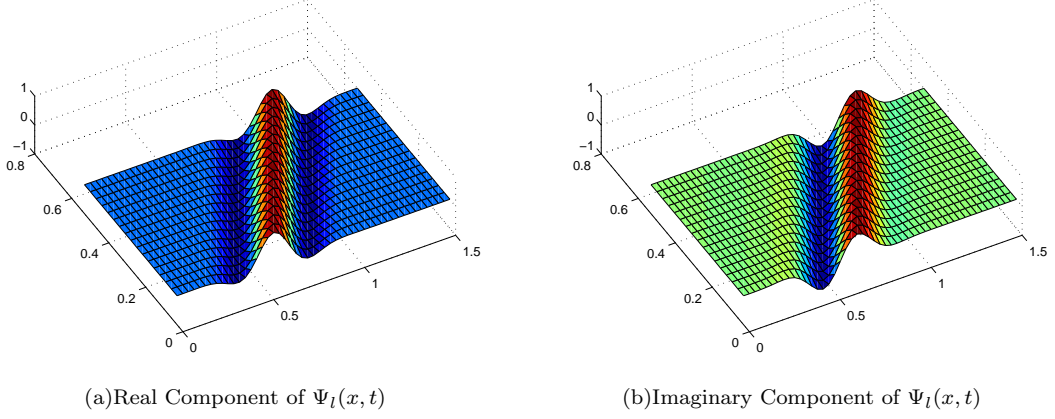


FIG. 1: Analytic Solution of the Massless Initial Value Problem

$$\begin{aligned}
\partial_x \Psi_{x,t} &= \frac{1}{2h} (\Psi_{x+h,t} - \Psi_{x-h,t}) \\
\partial_t \Psi_{x,t} &= \frac{1}{2h} (\Psi_{x,t+h} - \Psi_{x,t-h})
\end{aligned} \tag{9}$$

The central finite difference discretization was implemented using the bilinear form of the finite difference method shown in equation 7 and the initial value was introduced via a matrix partitioning scheme. The result of the balanced difference discretization when applied to the 1 + 1 dimensional Dirac initial value problem is shown by Figure 2 and Table I.

Figure 2 shows that the wave function is similar to the analytic solution when the space and time step sizes are equal. However, when unequal step sizes are used the wave shape deteriorates and is shifted rightward, indicating speeds in excess of the speed of light, which is physically impossible.

TABLE I: Numerical Performance of Central Difference Discretization

$\Omega = [0, 1.6] \times [0, 0.8]$			
$\Delta t = \Delta x$			
Mesh Size	Matrix Size	BICGSTAB Iterations	Error %
32×16	1122×1122	97.5	14.38%
48×24	2450×2450	120.5	6.28%
64×32	4290×4290	161	9.04%
80×40	6642×6642	418.5	15.37%
$\Delta t = 2\Delta x$			
64×16	2210×2210	129	76.79%
80×20	3402×3402	250	56.40%
96×24	4850×4850	307.5	34.36%
112×28	6554×6554	578.5	38.85%

Table I shows that L_2 norm of the error initially improves with a finer mesh, but does not improve uniformly and does not appear to tend toward zero with finer mesh spacings. Further, when the spacing is unequal, $\Delta t = 2\Delta x$, the error is substantially larger, which is expected due to its non-physical behavior.

B. Balanced Difference Discretization

When used to create an explicit propagator, the central difference discretization does not necessarily conserve the probability current of the wave-function. To address this shortcoming the partial derivative stencil in equation 9 is

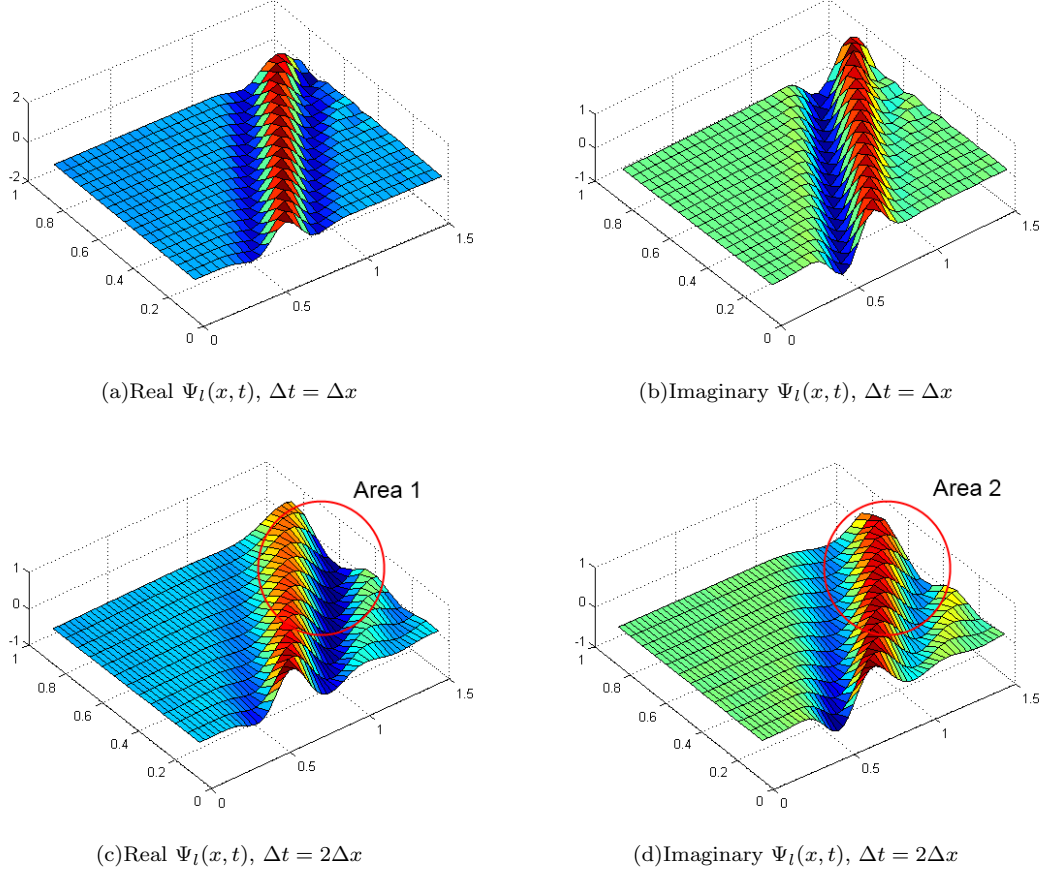


FIG. 2: Central Difference Solution. Note that in Area 1 and Area 2, the wave function has shifted rightward, indicating super-luminal propagation, which is forbidden for massless solutions of the Dirac equation

replaced by stencils that are arranged symmetrically with respect to space and time as follows [14].

$$\begin{aligned}\partial_x \Psi_{x,t} &= \frac{1}{4h} (\Psi_{x+h,t+h} + \Psi_{x+h,t-h} - \Psi_{x-h,t+h} - \Psi_{x-h,t-h}) \\ \partial_t \Psi_{x,t} &= \frac{1}{4h} (\Psi_{x+h,t+h} + \Psi_{x-h,t+h} - \Psi_{x+h,t-h} - \Psi_{x-h,t-h})\end{aligned}$$

Unlike the original paper [14], where this discretization is used to construct an explicit propagator, our implementation is fully implicit in both time and space.

Figure 3 shows that while the wave shape is choppy, when tested with equal time and space step sizes, it holds a continuous pattern in the overall shape of the analytic solution and the solution shows the correct propagation speed of $v = c$. However, with unequal space and time step sizes the propagation speed is visibly slowed to $v < c$.

C. Triangular Lagrangian Elements

Triangular Lagrangian finite elements represent one of the most commonly used shapes in the finite element method. In this case the nodes of the discrete Dirac equation are arranged on a grid pattern, so each square is composed of two triangular elements as shown in figure 4. Assuming the single grid element is a unit square with local variables x and t , the interpolation polynomials on triangle T_{123} are given by

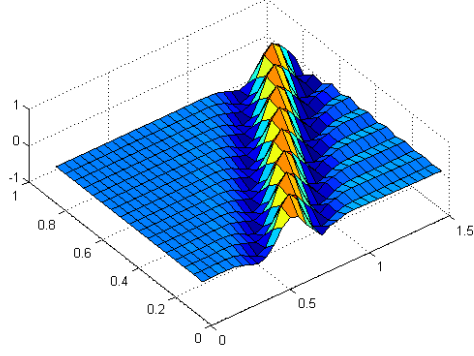
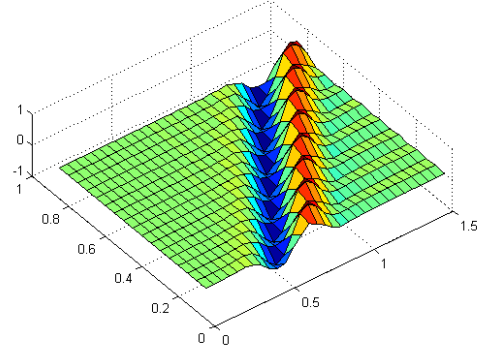
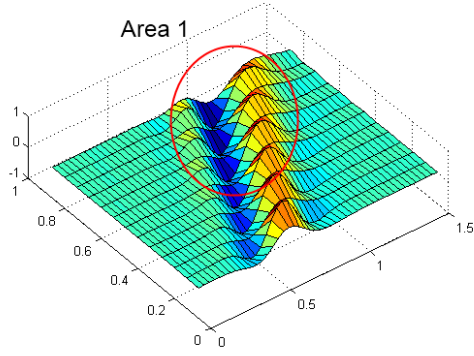
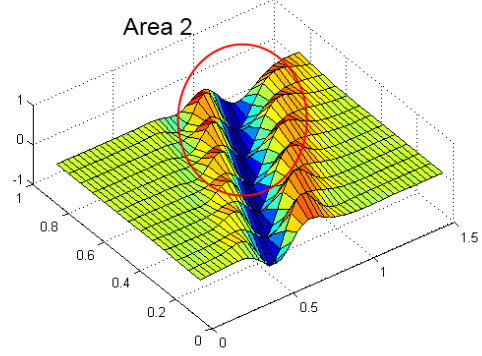
(a) Real $\Psi_l(x, t)$, $\Delta t = \Delta x$ (b) Imaginary $\Psi_l(x, t)$, $\Delta t = \Delta x$ (c) Real $\Psi_l(x, t)$, $\Delta t = 2\Delta x$ (d) Imaginary $\Psi_l(x, t)$, $\Delta t = 2\Delta x$

FIG. 3: Balanced Difference Solution. Note that in Area 1 and Area 2, the wavefunction has shifted leftward, indicating sub-luminal propagation, which is inconsistent with the expected behavior of massless solutions

TABLE II: Numerical Performance of Balanced Difference Discretization

$\Omega = [0, 1.6] \times [0, 0.8]$				
$\Delta t = \Delta x$				
Mesh Size	Matrix Size	BICGSTAB Iterations	Residual	Error %
32×16	1122×1122	120	.044	27.89%
48×24	2450×2450	863	.03	19.34%
64×32	4290×4290	53.5	.029	15.30%
80×40	6642×6642	65	.025	11.11%
$\Delta t = 2\Delta x$				
64×16	2210×2210	996	.13	75.76%
80×20	3402×3402	536	.03	60.29%
96×24	4850×4850	832	.26	45.36%
112×28	6554×6554	818	.34	38.94%

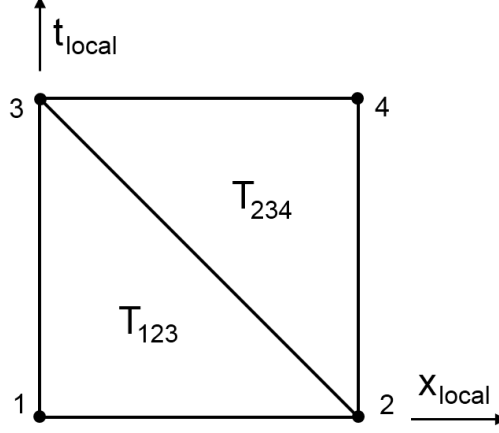


FIG. 4: Local Grid Square of a Triangular Finite Element Discretization

$$\left. \begin{aligned} n_1(x, t) &= 1 - x - t \\ n_2(x, t) &= x \\ n_3(x, t) &= t \end{aligned} \right\} \text{ for } (x, t) \in T_{123} \text{ and}$$

$$\left. \begin{aligned} n_1(x, t) &= 0 \\ n_2(x, t) &= 0 \\ n_3(x, t) &= 0 \end{aligned} \right\} \text{ for } (x, t) \text{ elsewhere}$$

similarly, interpolation polynomials for T_{234} are given by

$$\left. \begin{aligned} n_2(x, t) &= 1 - t \\ n_3(x, t) &= 1 - x \\ n_4(x, t) &= x + t - 1 \end{aligned} \right\} \text{ for } (x, t) \in T_{234} \text{ and}$$

$$\left. \begin{aligned} n_2(x, t) &= 0 \\ n_3(x, t) &= 0 \\ n_4(x, t) &= 0 \end{aligned} \right\} \text{ for } (x, t) \text{ elsewhere}$$

Evaluating the finite element the integral in equation 6 establishes an algebraic relationship between the nodes that for non-boundary elements is equivalent to a finite difference stencil. The finite difference stencil for triangular Lagrangian elements are calculated to be

$$\partial_x \rightarrow \frac{1}{36h} \begin{bmatrix} -1 & 1 & \\ -2 & 0 & 2 \\ & -1 & 1 \end{bmatrix} \quad \partial_t \rightarrow \frac{1}{36h} \begin{bmatrix} 1 & 2 & \\ -1 & 0 & 1 \\ & -2 & -1 \end{bmatrix} \quad (10)$$

The columns of the matrices above correspond to the spatial dimension x and the rows correspond to the temporal dimension t . It is apparent that the stencils above are not symmetric with respect to space and time. This means that the choice of element shape may bias the finite difference stencil along the characteristic line $x = t$ or $x = -t$, depending on which triangle orientation is chosen.

Figure 5 shows that instead of instability, first-order Lagrangian space-time finite elements lose wave amplitude very quickly and appear over-damped. From a physical perspective, the particle is disappearing into space. While the precise reason for this disappearance is unknown, it may be due to the finite difference stencils' bias in the opposite direction of particle propagation. When unequal step sizes in space and time were tested, the wave function begins to move to the left in the opposite direction of the analytic solution and at a speed greater than the speed of light.

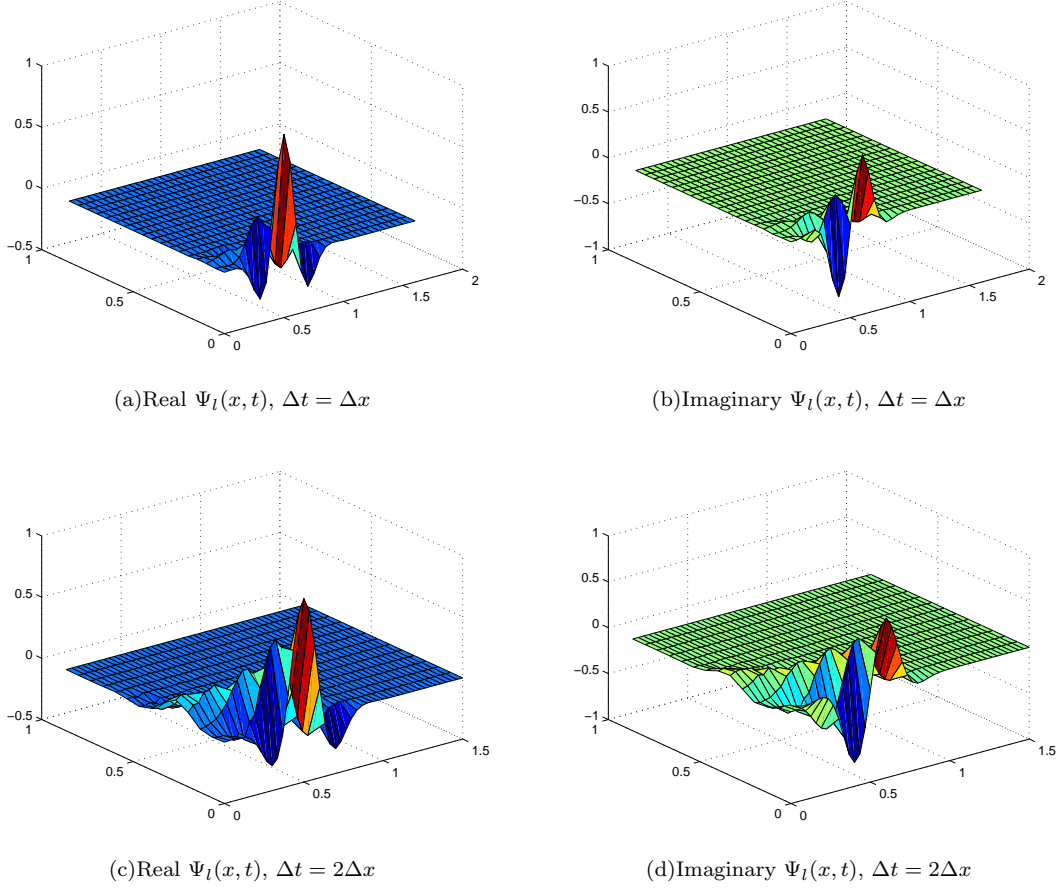


FIG. 5: Triangular Lagrangian Element Solution. Note that the calculated wave fades out quickly and propagates in the wrong direction, compared with the analytic solution.

IV. TENSOR ELEMENT BASED APPROACHES

In this section we will show three space-time discretizations that use square shaped "tensor" finite elements along with a selected basis function space to form the weak Dirac boundary value problem. Each of these approaches shows overall convergence to the shape of the analytic solution without the presence of superluminal, subluminal, or counter-directional wave functions that were present with the previous approaches.

A. Polynomial Hermite Tensor Elements

These functions are conceptually related to the third-order piecewise Hermite interpolation polynomials given by

$$\mathbf{H}(e) = \begin{cases} H_{00}(e) = (1 + 2e)(1 - e)^2 \\ H_{10}(e) = 6e(1 - e)^2 \\ H_{01}(e) = e^2(3 - 2e) \\ H_{11}(e) = 6e^2(e - 1) \end{cases}$$

We use the tensor product $\mathbf{H}(x) \times \mathbf{H}(t)$ to create a composite function that has C^1 continuity in a two dimensional plane, which is required for analytic solutions in quantum mechanics. This set also allows the set of second-order mixed partials to be varied independently. However, the continuity of mixed partials has no special physical significance in this case, so these functions are removed in order to reduce the degrees of freedom present in the discrete system.

TABLE III: Numerical Performance of Triangular Lagrangian Elements

$\Omega = [0, 1.6] \times [0, 0.8]$			
$\Delta t = \Delta x$			
Mesh Size	Matrix Size	BICGSTAB Iterations	Error %
32×16	1122×1122	2.5	101.6%
48×24	2450×2450	2.5	100.9%
64×32	4290×4290	2.5	100.6%
80×40	6642×6642	2.5	100.4%
$\Delta t = 2\Delta x$			
64×16	2210×2210	5	108.45%
80×20	3402×3402	7	108.93%
96×24	4850×4850	4	106.06%
112×28	6554×6554	4	105.49%

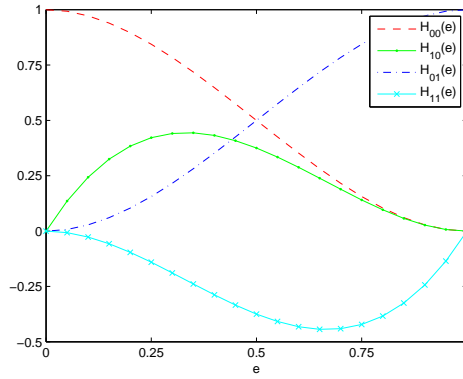
FIG. 6: C^1 Hermite basis functions where $k = 3$.

Figure 7 shows that when Hermite tensor elements are used as a function space for the given initial value problem, the overall behavior of the wave-function is consistent with the analytic solution both when $\Delta t = \Delta x$ and when $\Delta t = 2\Delta x$, although the error function is substantial.

TABLE IV: Numerical Performance of Hermite Tensor Element Discretization

$\Omega = [0, 1.6] \times [0, 0.8]$			
$\Delta t = \Delta x$			
Mesh Size	Matrix Size	BICGSTAB Iterations	Error %
30×15	2976×2976	961	21.92%
40×20	5166×5166	1801	25.64%
50×25	7956×7956	2888	16.09%
60×30	11346×11346	4221	10.97%
70×35	15336×15336	5113	7.35%
80×40	19926×19926	6186	8.81%

B. Trigonometric Hermite Tensor Elements

Here we will chose our basis functions for the finite element vectors Ψ to be C^1 trigonometric functions given by

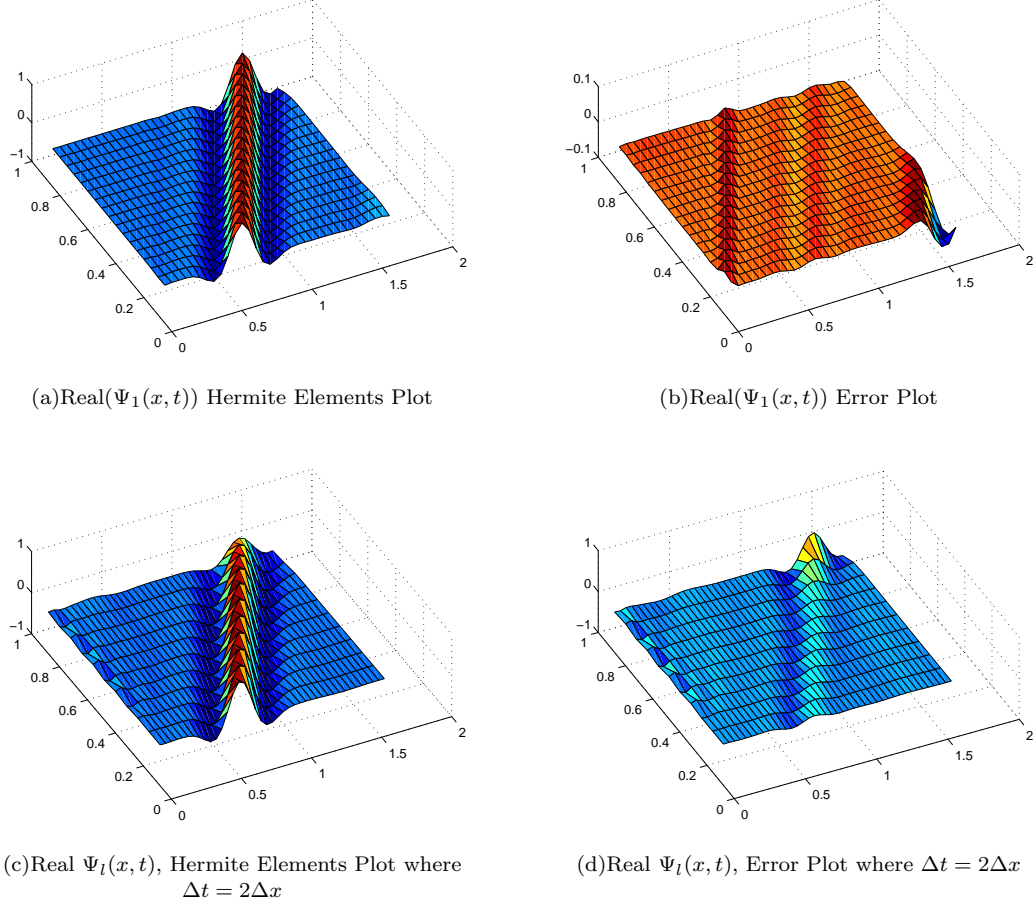


FIG. 7: Solution Curve of Polynomial Hermite Tensor Element

$$\mathbf{N}(e) = \begin{cases} n_{00}(e) = \cos^2(\frac{\pi e}{2}) \\ n_{10}(e) = k \cos(\frac{\pi e}{2}) \sin(\pi e) \\ n_{01}(e) = \sin^2(\frac{\pi e}{2}) \\ n_{11}(e) = -k \sin(\frac{\pi e}{2}) \sin(\pi e) \end{cases}$$

These are conceptually similar to the Hermite polynomials. As previously, we use the tensor product $\mathbf{N}(x) \times \mathbf{N}(t)$ to create a composite function that has C^1 continuity.

From viewing the solution and error plot in figure 8 we can see that although the overall shape of the solution is very similar to the analytic solution the error wave is relatively large.

C. Linear Lagrangian Tensor Elements

The function space of the linear Lagrangian elements is formed from the tensor product of the first order Lagrangian interpolation polynomials in the x and t directions. Since they are first order, there is only one degree of freedom per node, or four degrees of freedom per tensor element, making this element type much simpler than the previous elements shown.

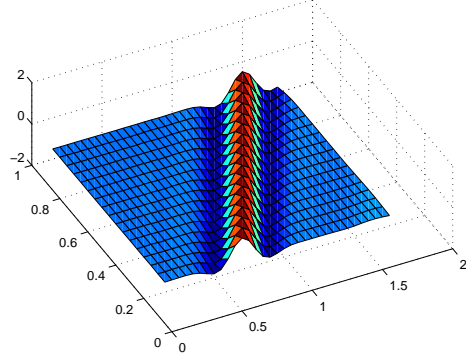
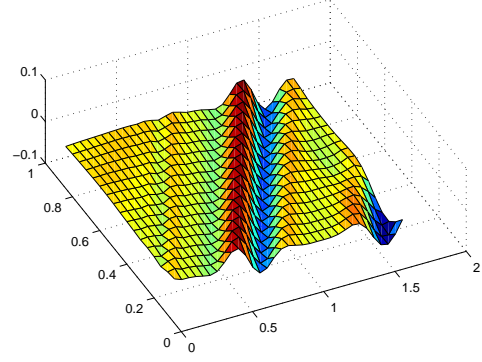
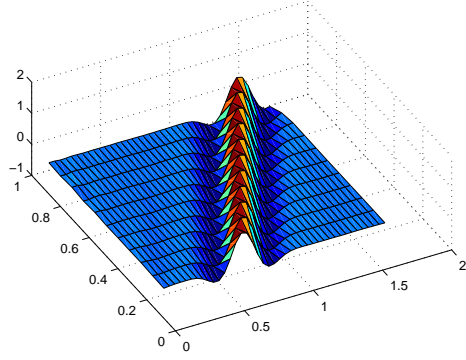
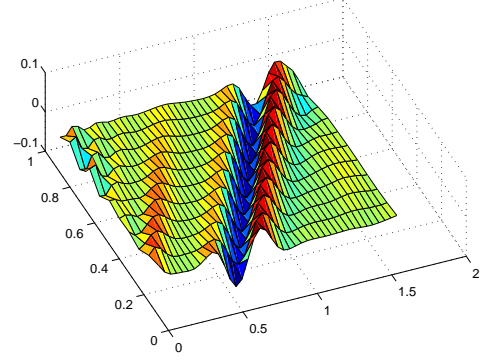
(a) $\text{Real}(\Psi_1(x, t))$ Trigonometric Elements Plot(b) $\text{Real}(\Psi_1(x, t))$ Error Plot(c) $\text{Real}(\Psi_1(x, t))$ Trigonometric Elements Plot where $\Delta t = 2\Delta x$ (d) $\text{Real}(\Psi_1(x, t))$ Error Plot where $\Delta t = 2\Delta x$

FIG. 8: Solution Curve of Trigonometric Tensor Element

TABLE V: Numerical Performance of Trigonometric Tensor Element Discretization

$\Omega = [0, 1.6] \times [0, 0.8]$			
$\Delta t = \Delta x$			
Mesh Size	Matrix Size	BICGSTAB Iterations	Error %
30×15	2976×2976	1098	6.87%
40×20	5166×5166	1992	5.15%
50×25	7956×7956	3021	4.19%
60×30	11346×11346	4375	3.69%
70×35	15336×15336	5339	3.50%
80×40	19926×19926	6238	3.18%

The Lagrangian interpolation polynomials are given by the following expression.

$$\begin{aligned}
 n_1(x, t) &= (l - x)(1 - t) \\
 n_2(x, t) &= x(1 - t) \\
 n_3(x, t) &= (x - 1)t \\
 n_4(x, t) &= xt
 \end{aligned}$$

From Figure 9 we see that the Lagrangian tensor elements also produce a numerical result very close to the analytic solution. This behavior is consistent both when $\Delta t = \Delta x$ and when $\Delta t = 2\Delta x$.

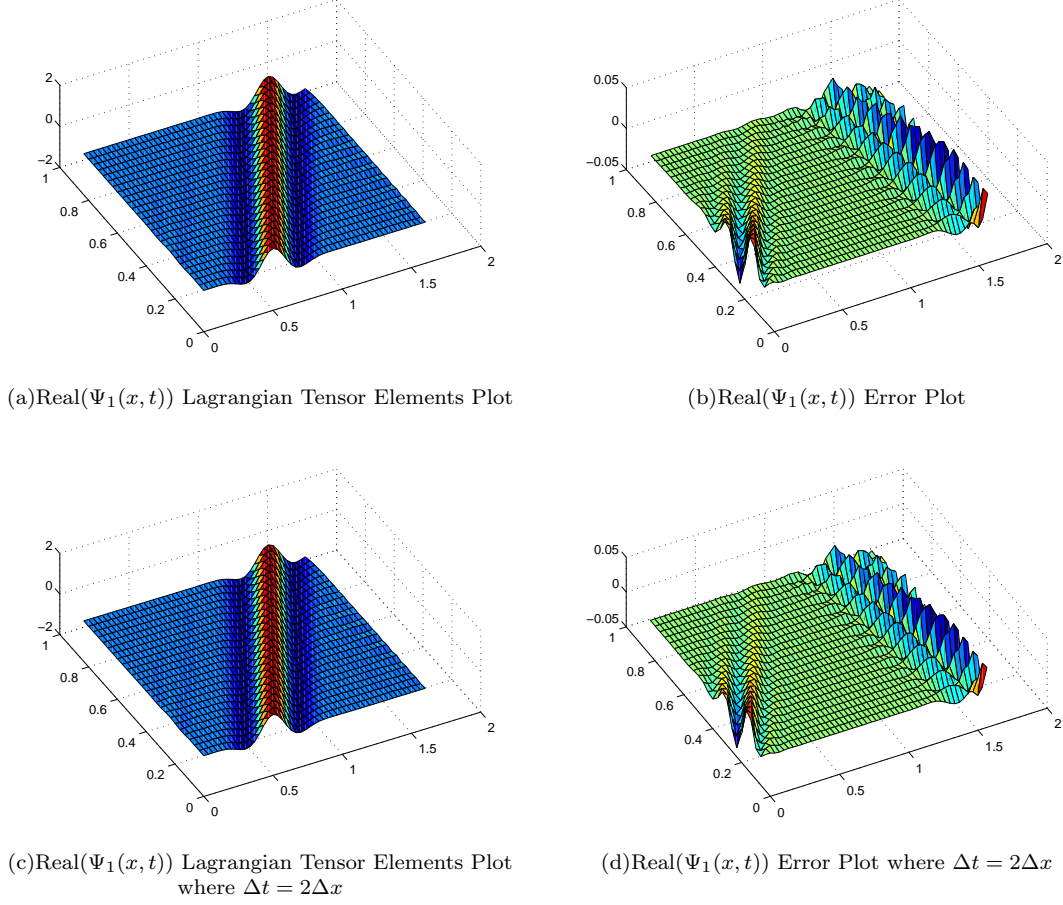


FIG. 9: Solution Curve of Lagrangian Tensor Element

TABLE VI: Numerical Performance of Lagrangian Tensor Elements

$\Omega = [0, 1.6] \times [0, 0.8]$			
$\Delta t = \Delta x$			
Mesh Size	Matrix Size	BICGSTAB Iterations	Error %
48×24	2450×2450	331	4.64%
64×32	4290×4290	679	2.86%
80×40	6642×6642	899	2.22%
96×48	9506×9506	1230	3.07%
112×56	12882×12882	1569	3.49%
128×64	16770×16770	2012	7.67%

Table VI shows that the Lagrangian tensor elements have substantially lower error, smaller matrix size, greater mesh refinement and more efficient convergence than either the Hermite or trigonometric tensor elements. Unfortunately, the L_2 norm of the error actually increases with greater mesh refinement. Possible sources of this remaining error will be analyzed in the following section.

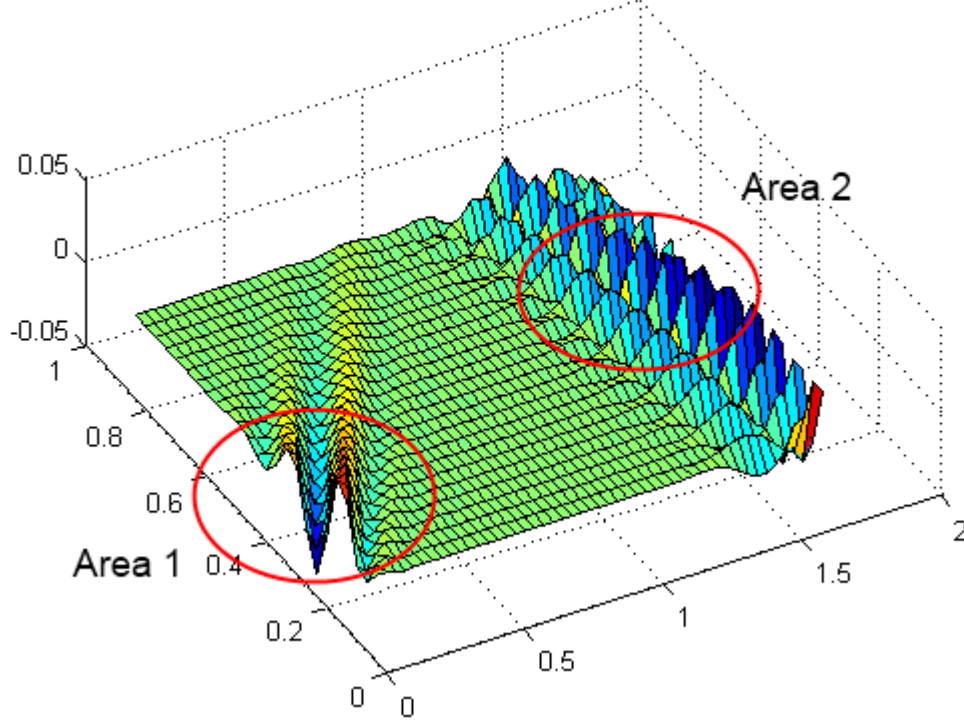


FIG. 10: Error Analysis of Lagrangian Tensor Element. In Area 1 we see boundary error that propagates inward from the natural boundary conditions on the right, left, and rear edges of the domain. In Area 2 the error wave is composed of closely spaced peaks of period $2h$, which are effectively invisible to the partial derivative operator for non-boundary nodes

D. Error Analysis of Linear Lagrangian Tensor Elements

From looking at the error wave in figure 9 and the analysis in figure 10 we make the following observations about the sources of error. The first source of error for Lagrangian tensor elements may lie in the stencil of the ∂_x and ∂_t operators. For non-boundary nodes, linear Lagrangian tensor elements introduce the following algebraic relationship between nodes.

$$\partial_x \rightarrow \frac{1}{12h} \begin{bmatrix} -1 & 0 & 1 \\ -4 & 0 & 4 \\ -1 & 0 & 1 \end{bmatrix} \quad \partial_t \rightarrow \frac{1}{12h} \begin{bmatrix} 1 & 4 & 1 \\ 0 & 0 & 0 \\ -1 & -4 & -1 \end{bmatrix}$$

It is apparent that the value of the partial derivative as calculated by these operators would approach zero as the period of the wave approaches $2h$. The error wave across the right-hand side appears to have a period of exactly $2h_t$, making it "invisible" to the discrete form of our partial derivative operator.

A second source of error may come from the boundary conditions across both sides $x = 0$ and $x = x_{max}$. Here an error wave springs *ex-nihilo* from the $x = 0$ side and propagates parallel to the solution. It may be possible to eliminate such waves by choosing Dirichlet boundary conditions. However, these conditions would imply knowledge solution before the solution is calculated. The source of this problem is that the domain sides are not completely contained by the light-cone of our initial condition.

If the domain were sufficiently wide as to preclude the wave from reaching the boundary, it would then be appropriate to apply Dirichlet boundary conditions to the sides of the experiment. However, this would also add significant empty space to the domain and computational cost to the experiment.

From the error observations above we draw the following conclusions. One, boundary conditions should utilize light cone causality to ensure a unique solution. Two, momentum and energy operators should be able to detect tightly spaced, erroneous wave patterns and prevent them from appearing in the solution..

V. DIAMOND SHAPED TENSOR ELEMENTS

In order to reduce the error waves observed in the Lagrangian tensor element discretization, we propose the following element shape for discretizing the 1+1 Dirac equation, shown in Figure 11. The $x - t$ plane is rotated 45° to create two new axis that will name "right" and "left". This shape gives us two important advantages.

One, we may impose Dirichlet boundary conditions across both the right and left axis. The entire domain is then contained within the light cone of the "initial" conditions, meaning that the solution should be unique, at least from the physical perspective, since no new information can enter the domain. This is shown graphically in figure 11(a).

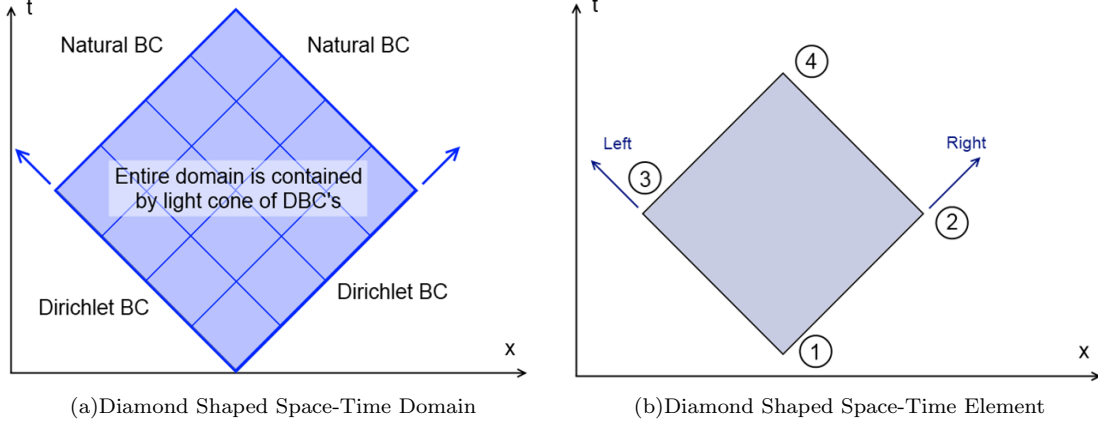


FIG. 11: Diamond Shaped Domain and Single Element Composition

Linear interpolation polynomials for the diamond tensor elements may be defined as follows.

$$\begin{aligned}
 n_1(r, l) &= (l - r)(1 - l) \\
 n_2(r, l) &= r(1 - l) \\
 n_3(r, l) &= (r - 1)l \\
 n_4(r, l) &= rl
 \end{aligned}$$

Two, the partial derivative stencils now become more complex and should be better able to detect the closely chopped error waves that were present in the Lagrangian tensor element solution. For non-boundary elements, these linear interpolation polynomials introduce the following algebraic relationship between nodes for the two partial derivative operators of the Dirac equation.

$$\partial_x \rightarrow \frac{1}{h} \begin{bmatrix} & & 0 \\ & -\frac{1}{3} & +\frac{1}{3} \\ -\frac{1}{6} & 0 & +\frac{1}{6} \\ & -\frac{1}{3} & +\frac{1}{3} \\ & 0 & \end{bmatrix} \quad \partial_t \rightarrow \frac{1}{h} \begin{bmatrix} & +\frac{1}{6} & \\ +\frac{1}{3} & 0 & +\frac{1}{3} \\ 0 & -\frac{1}{3} & -\frac{1}{3} \\ & -\frac{1}{6} & 0 \end{bmatrix}$$

Using this domain, element shape, and interpolation polynomial set with the weak form defined in equation 6 generates the following solution shape shown in Figure 12. The magnitude of the error wave is extremely small when compared to the solution, and shows that the finite element solution is nearly exact when one considers the values of the wave-function at the node points. The scale of the error at the nodes is around twelve orders of magnitude lower than the error at the nodes for other methods considered.

We note that the solution shows substantially lower error when compared to any of the methods previously presented. This is further confirmed by our results in VII. Here we see that the L_2 norm of the error is much lower than for the other methods tested, and that the numerical simulation converged more quickly as well. In the case of a the 64×128 element matrix the diamond tensor element solution converged in 1897 iterations versus 2012 iterations for the Lagrangian tensor elements, and the L_2 norm of the error was 0.18% (Table VII) for the diamond tensor elements versus 7.67% (Table VI) for the Lagrangian tensor elements.

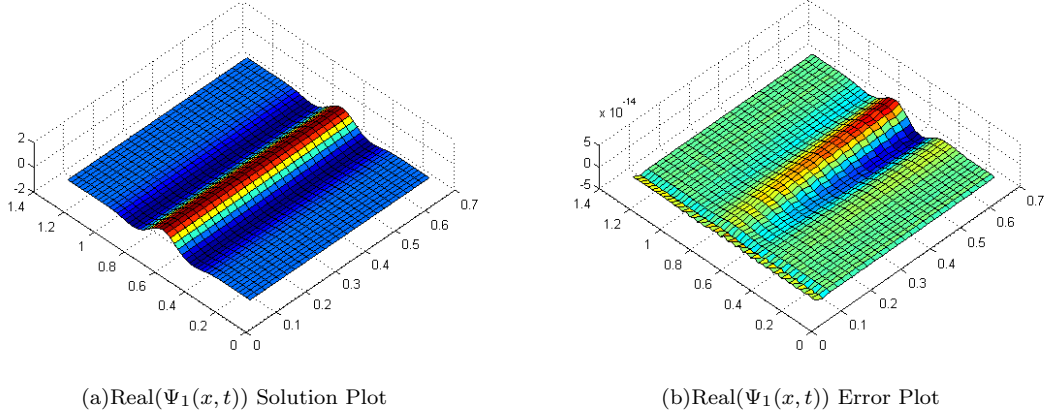


FIG. 12: Solution Curve of Diamond Lagrangian Tensor Element. Note the reduction in error scale compared with previous methods tested

TABLE VII: Numerical Performance of Diamond Tensor Elements

$\Omega = [0, 1.2] \times [0, 0.8]$			
$\Delta t = \Delta x$			
Mesh Size	Matrix Size	BICGSTAB Iterations	Error %
24×48	2450×2450	305	1.28%
32×64	4290×4290	621	0.71%
40×80	6642×6642	883	0.46%
48×96	9506×9506	1177	0.32%
56×112	12882×12882	1593	0.23%
64×128	16770×16770	1897	0.18%

Finally, as with the other space-time tensor element approaches, no superluminal or subluminal behavior was observed when tested with unequal space and time spacings.

A. Rotation Tests

To test the effectiveness of other possible domain rotation angles, the domain $\Omega \times [0, T]$ was rotated about the origin counter-clockwise from $\theta = 0^\circ$ to $\theta = 45^\circ$. This is shown conceptually in Figure 13 demonstrating how the domain rotates about the origin of the space-time plain.

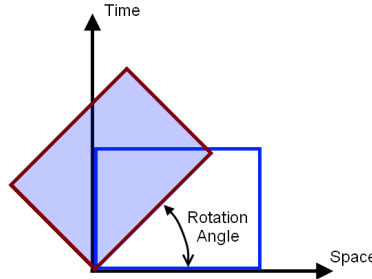


FIG. 13: Conceptual Diagram of a Domain Rotation in Space-Time

After performing this rotation on the domain, a similar initial value problem as the one given in 6 was then solved

on the new rotated domain. The algebraic formulation rotated domain is given below.

$$\begin{aligned}
 D\hat{\Psi}(x', t') &= 0 \\
 \hat{\Psi}(\cdot, 0') &= \Psi^0 \\
 \text{where } \begin{bmatrix} x' \\ t' \end{bmatrix} &= \begin{bmatrix} \cos(\theta) & -\sin(\theta) \\ \sin(\theta) & \cos(\theta) \end{bmatrix} \begin{bmatrix} x \\ t \end{bmatrix} \\
 \text{and } [0 < x < x_{max}], [0 < t < t_{max}]
 \end{aligned}$$

In this test, $t_{max} = .4$ and $x_{max} = \frac{2}{3} * \sec(45^\circ - \theta)$, where θ is the angle of rotation. The x -axis is scaled by a factor of $\sec(45^\circ - \theta)$ so that the wave function remains centered in the domain throughout the rotation. This rotation has the added advantage of following the path of the solution more closely, since high-energy, low mass solutions to the Dirac equation tend to move along the characteristic lines of equation; which is to say, particles that have high energy and low mass move at nearly the speed of light.

This test was also conducted with non-zero masses, and results compared to a solution calculated using numerical Fourier transformation. Due to stability concerns in the massive case, a Dirichlet boundary condition was added to the side $x = 0$ and the center of the wave function was moved from $x = 0.5$ to $x = 0.8$ to keep the wave function from colliding with the Dirichlet boundary condition on the $x = 0$ wall. The domain shape was slightly altered to $[0 \leq x \leq 1.6] \times [0 \leq t \leq .4]$.

The number of GMRES iterations and the L_2 norm of the error were recorded and plotted against the rotation angle used. The results are shown in Figure 15 and 14.

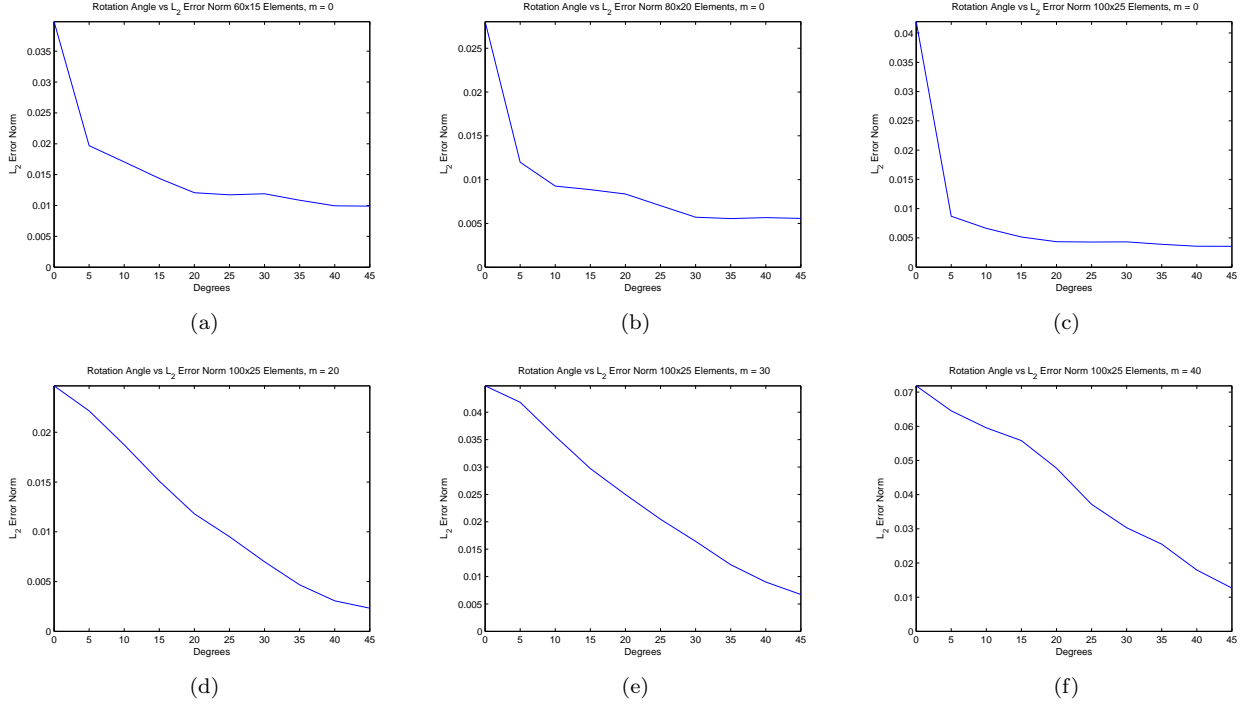


FIG. 14: $|\Psi - \Psi_{FEM}|_2$, the L_2 Error Norm of the Computed Wave Function vs the Angle of Rotation

In Figure 14 the L_2 norm of the error is shown to decrease steadily as the angle is increased from 0° to 45° and reaches its lowest point at 45° . This relationship is demonstrated in each case tested, regardless of particle mass.

Likewise, in Figure 15 the number of GMRES iterations is shown to decrease steadily as the angle is increased from 0° to 45° and reaches its lowest point at 45° . This relationship is demonstrated for each domain size tested but only in the massless case.

Interestingly, this relationship is changed somewhat as the mass increases. At a mass of $m = 20$ and $m = 30$, the fewest iterations are used at around 40° . When $m = 40$, the fewest iterations are required at 35° . Finding the source of this small off-angle efficiency improvement requires further investigation.

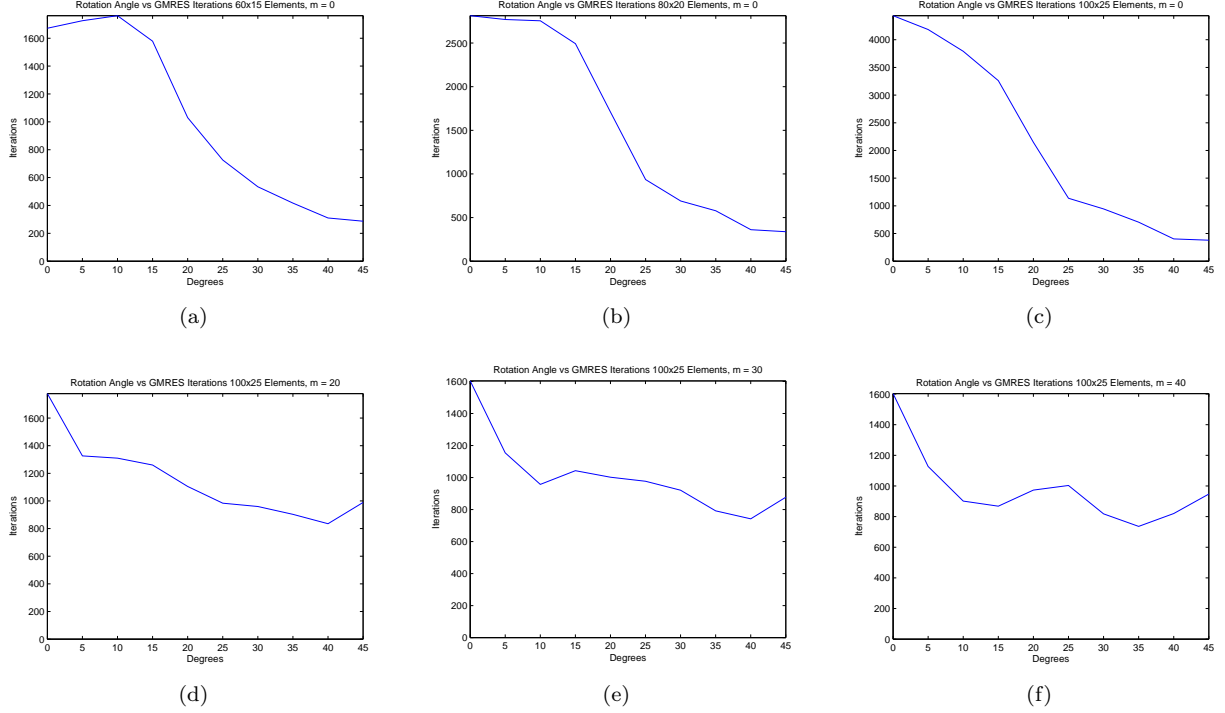


FIG. 15: GMRES iterations to reach a residual of 10^{-6} vs the Angle of Rotation

These results demonstrate that a 45° rotation in space-time shows the lowest error for all angles and mass levels tested. Further, they also demonstrate that a 45° rotation is either optimal or nearly optimal from a GMRES iterations perspective; however, this relationship is less straightforward than the correlation with error and will require further research to establish the relationship between the massive particle and the optimal rotation angle for algorithmic efficiency.

VI. CONCLUSION

From the data above we have shown several space-time approaches that may be useful in numerical calculations of the Dirac equation in a rectangular space-time domain. We have also shown that a physically-motivated selected of element and domain shape can substantially improve performance and reduce error for the numerical experiments considered above. Since this improvement was shown for an equation dominated by first-order operators, it may be possible to use a similar approach for other equations with unstable first-order operators as well.

The results above also show that problems with super-luminal and physically inconsistent propagation may be addressed by choice of discretization and using a fully implicit method. This is then corrected without reference to the problem of Fermion doubling as was suggested by Müller et al. in [13].

To expand the usefulness of this numerical approach, further research should be conducted in several areas. One, the sample problem should be developed for $2+1$ and $3+1$ dimensional settings. Two, a more formal error analysis should be conducted to understand the root cause of the simulation behavior above. Three, scalable preconditioners should be investigated for new numerical solutions to the Dirac equation, especially given the size of Dirac-based problems in $3+1$ dimensions (or more). Finally, this model should be tested for suitability and performance in more realistic, inhomogeneous or nonlinear settings.

Acknowledgements We thank you to Professor Dongming Mei from the Department of Physics of University of

South Dakota for his discussion on physics interpretation on this results.

-
- [1] Andre D. Bandrauk Francois Fillion-Gourdeau, Emmanuel Lorin. Numerical solution of the time-dependent dirac equation in coordinate space without fermion-doubling. *arXiv:1107.4650v2*, 2012.
 - [2] A Widom and YN Srivastava. Neutrino flavor oscillations using the dirac equation. *arXiv preprint hep-ph/9608476*, 1996.
 - [3] Kenneth G. Wilson. Confinement of quarks. *Phys. Rev. D*, 10:2445–2459, Oct 1974.
 - [4] T. Sakurai, H. Tadano, and Y. Kuramashi. Application of block krylov subspace algorithms to the wilsondirac equation with multiple right-hand sides in lattice qcd. *Computer Physics Communications*, 181(1):113 – 117, 2010.
 - [5] Y. Nakamura, K.-I. Ishikawa, Y. Kuramashi, T. Sakurai, and H. Tadano. Modified block bicgstab for lattice qcd. *Computer Physics Communications*, 183(1):34 – 37, 2012.
 - [6] Martin Lüscher. Solution of the dirac equation in lattice qcd using a domain decomposition method. *Computer Physics Communications*, 156(3):209 – 220, 2004.
 - [7] H.B. Nielsen and M. Ninomiya. A no-go theorem for regularizing chiral fermions. *Physics Letters B*, 105(23):219 – 223, 1981.
 - [8] S. Chandrasekharan and U.-J. Wiese. An introduction to chiral symmetry on the lattice. *Progress in Particle and Nuclear Physics*, 53(2):373 – 418, 2004.
 - [9] Hasan Almanasreh and Nils Svanstedt. G-convergence of dirac operators. *Journal of Function Spaces and Applications*, 2012.
 - [10] O. Kullie, D. Kolb, and A. Rutkowski. Two-spinor fully relativistic finite-element (fem) solution of the two-center coulomb problem. *Chemical Physics Letters*, 383(34):215 – 221, 2004.
 - [11] O. Kullie and D. Kolb. High accuracy dirac-finite-element (fem) calculations for H_2^+ and Th_2^{179+} . *The European Physical Journal D - Atomic, Molecular, Optical and Plasma Physics*, 17:167–173, 2001.
 - [12] J.P. Desclaux, J. Dolbeault, M.J. Esteban, P. Indelicato, and E. Sr. Computational approaches of relativistic models in quantum chemistry. In C. Le Bris, editor, *Special Volume, Computational Chemistry*, volume 10 of *Handbook of Numerical Analysis*, pages 453 – 483. Elsevier, 2003.
 - [13] N. Grün C. Müller and W. Scheid. Finite element formulation of the dirac equation and the problem of fermion doubling. *Physics Letters A*, 242(45):245 – 250, 1998.
 - [14] P. P. F. Wessels, W. J. Caspers, and F. W. Wiegell. Discretizing the one-dimensional dirac equation. *EPL (Europhysics Letters)*, 46(2):123, 1999.

Appendix A: Solution of the Initial Value Problem

This discussion follows closely to the derivation presented in the appendices of [1]. In order to compare our results with known solutions of the Dirac equation, we will first consider the case of the massless Dirac equation. Since we are interested in the behavior of particles whose mass is very close to zero, this should give us some indication of the fitness of our approach for real-world problems.

Removing the mass term from equation 1 and multiplying both sides by the matrix $\begin{bmatrix} 1 & 0 \\ 0 & -1 \end{bmatrix}$ gives us the following equation.

$$\left(i\hbar \begin{bmatrix} 1 & 0 \\ 0 & 1 \end{bmatrix} \partial_t + i\hbar \begin{bmatrix} 0 & -1 \\ -1 & 0 \end{bmatrix} \partial_x \right) \begin{bmatrix} \Psi_l(x, t) \\ \Psi_r(x, t) \end{bmatrix} = 0$$

We then make the following substitutions

$$\begin{bmatrix} 1 & 0 \\ 0 & 1 \end{bmatrix} = I \quad \begin{bmatrix} 0 & -1 \\ -1 & 0 \end{bmatrix} = -\sigma_1 \quad \begin{bmatrix} \Psi_l(x, t) \\ \Psi_r(x, t) \end{bmatrix} = \Psi(x, \tau)$$

and rearrange the equation as follows.

$$-i\hbar I \partial_t \Psi(x, \tau) = -i\hbar c \sigma_1 \partial_x \Psi(x, \tau) \tag{A1}$$

We may further simplify this equation into a first order ODE by taking the Fourier transform with respect to $\hbar\omega = p$ which expresses the massless Dirac operator in momentum space.

$$-i\hbar I \partial_t \Psi(p, \tau) = \sigma_1 p_x \Psi(p, \tau) \quad (\text{A2})$$

Integrating directly from $\tau = 0$ to $\tau = t$ gives us the general solution to the massless initial value problem in momentum space.

$$\Psi(p, t) = e^{(\frac{i}{\hbar} \sigma_1 p_x t)} \Psi_0(p)$$

Where we may then apply Euler's Identity in order to remove the matrix from the exponential

$$\Psi(p, t) = \left(I \cos\left(\frac{p_x}{\hbar} t\right) + i \sigma_1 \sin\left(\frac{p_x}{\hbar} t\right) \right) \Psi_0(p) \quad (\text{A3})$$

Where I is the 2×2 identity matrix. If we take our initial function to be a Gaussian wave of the form $\Psi(x, 0) = \begin{bmatrix} e^{(i\pi b x - (ax)^2)} \\ e^{(i\pi b x - (ax)^2)} \end{bmatrix}$ which may be expressed in momentum space as $\hat{\Psi}_0(p) = \begin{bmatrix} (2a^2)^{-\frac{1}{2}} e^{-\frac{(\omega + \pi b)^2}{4a^2}} \\ (2a^2)^{-\frac{1}{2}} e^{-\frac{(\omega + \pi b)^2}{4a^2}} \end{bmatrix}$. Inverting the Fourier transform from equation A3 with the given initial value results in the general initial value solution:

$$\Psi(x, t) = \begin{bmatrix} A & B \\ C & D \end{bmatrix} \begin{bmatrix} \Psi_1(x, 0) \\ \Psi_2(x, 0) \end{bmatrix} \quad (\text{A4})$$

where the values A , B , C , and D are define as

$$\begin{aligned} A &= \frac{1}{2} (e^{-a^2(t^2 - 2xt) - ib\pi t} + e^{-a^2(t^2 + 2xt) + ib\pi t}) \\ B &= \frac{1}{2} (-e^{-a^2(t^2 - 2xt) - ib\pi t} + e^{-a^2(t^2 + 2xt) + ib\pi t}) \\ C &= \frac{1}{2} (-e^{-a^2(t^2 - 2xt) - ib\pi t} + e^{-a^2(t^2 + 2xt) + ib\pi t}) \\ D &= \frac{1}{2} (e^{-a^2(t^2 - 2xt) - ib\pi t} + e^{-a^2(t^2 + 2xt) + ib\pi t}) \end{aligned}$$

Equation A4 may then be used to calculate the analytic solution to any combination of massless Gaussian wave packets with the packet width given by a and the momentum set by b .